Orbital-differentiated coherence-incoherence crossover identified by photoemission spectroscopy in LiFeAs

H. Miao,[1,2] Z. P. Yin,[3,4] S. F. Wu,[1] J. M. Li,[1] J. Ma,[1] B.-Q. Lv,[1] X. P. Wang,[1,5,6] T. Qian,[1] P. Richard,[1,5,7,*] L.-Y. Xing,[1] X.-C. Wang,[1] C. Q. Jin,[1,5] K. Haule,[3] G. Kotliar,[2,3] and H. Ding[1,5,7,†]

[1]*Beijing National Laboratory for Condensed Matter Physics, Institute of Physics, Chinese Academy of Sciences, Beijing 100190, China*
[2]*Condensed Matter Physics and Materials Science Department, Brookhaven National Laboratory, Upton, New York 11973, USA*
[3]*Department of Physics and Astronomy, Rutgers University, Piscataway, New Jersey 08854, USA*
[4]*Department of Physics and the Center of Advanced Quantum Studies, Beijing Normal University, Beijing 100875, China*
[5]*Collaborative Innovation Center of Quantum Matter, Beijing 100190, China*
[6]*Department of Physics, Tsinghua University, Beijing 100084, China*
[7]*School of Physical Sciences, University of Chinese Academy of Sciences, Beijing 100190, China*

In iron-based superconductors (FeSCs), orbital differentiation is an important phenomenon, whereby correlations stronger on the d_{xy} orbital than on the d_{xz}/d_{yz} orbital yield quasiparticles with a d_{xy} orbital character having larger mass renormalization and an abnormal temperature evolution. However, the physical origin of this orbital differentiation is debated between the Hund's coupling-induced unbinding of spin and orbital degrees of freedom and the Hubbard interaction instigated orbital-selective Mott transition. Here we use angle-resolved photoemission spectroscopy to identify an orbital-dependent correlation-induced quasiparticle (QP) anomaly in LiFeAs. The excellent agreement between our photoemission measurements and first-principles many-body theory calculations shows that the orbital-differentiated QP lifetime anomalies in LiFeAs are controlled by the Hund's coupling.

Understanding the origin of electronic correlations in high-temperature superconductors is a key step towards uncovering the pairing mechanism of their unconventional superconductivity [1–6]. Unlike copper oxide superconductors, where the electronic correlations are controlled by an on-site Hubbard-U interaction, the multiorbital and multiband nature of iron-based superconductors (FeSCs) poses a strong challenge to forming a clear picture of their strong orbital-dependent electronic correlations. In one scenario the electronic correlations arise because the FeSCs are in close proximity to a Mott state or an orbital-selective Mott state [7–10], where the Fe $3d$ orbitals are decoupled from each other and therefore their correlation strength is controlled by the Hubbard-U interaction, as in copper oxides [10]. In an alternative scenario the electronic correlations come mainly from the formation of large fluctuating local moments due to the Hund's rule coupling [11,12]. For this reason, FeSCs are dubbed Hund's metals [11]. In this Rapid Communication, we use high-resolution angle-resolved photoemission spectroscopy (ARPES) to measure the quasiparticle (QP) self-energy $\Sigma(k,\omega)$ and its temperature evolution, and compare them with first-principles density functional theory plus dynamical mean field theory (DFT+DMFT) calculations to clarify the origin of the many-body correlations in FeSCs.

High-quality single crystals of LiFeAs were synthesized by the self-flux method [13]. High-resolution ARPES data were recorded at the Institute of Physics, Chinese Academy of Sciences, using the He $I\alpha$ ($h\nu = 21.218$ eV) resonance line of a helium discharge lamp. The angular and momentum resolutions were set to $0.2°$ and 3 meV, respectively. ARPES polarization-dependent measurements were performed at the

Dreamline of Shanghai Synchrotron Light Source using a Scienta D80 analyzer with energy and momentum resolutions set to $0.2°$ and 10 meV, respectively. The photon energy 74 eV is selected to tune the $k_z = 0$. To select specific orbitals, we employed linearly polarized light to the mirror plane of the sample. All samples were cleaved *in situ*. The data were recorded in a vacuum better than 3×10^{-11} Torr with a discharge lamp and 10^{-10} Torr with a synchrotron light source. The normalization curve of the spectra is obtained by integrating the ARPES intensity in the whole measured energy range (-200 to 150 meV in our study), which covers most of the spectral weight in LiFeAs. Our calculations are performed using an *ab initio* theoretical method for correlated electron materials, based on a combination of DMFT and density functional theory (DFT) [12,14,15]. The calculation is performed at k_z close to the experimental value. This computational method improves the DFT description of the electronic structure of FeSCs, predicts the correct magnitude of the ordered magnetic moments [11], and improves the description of electronic spectral functions, Fermi surfaces [11,12], charge response functions such as the optical conductivity [12], and spin dynamics [16]. For the sake of consistency, we use in this work the same crystal structure, Hubbard **U** = 5.0 eV, Hund's $J_H = 0.8$ eV as in previous work [11,16].

LiFeAs ($T_c = 18$ K) offers an excellent platform for the study of QPs and the underlying many-body correlations. First, it is free of doping impurities, disorder, and has well-separated band dispersions [13,17,18], which is crucial to directly study the intrinsic QP dynamics. Second, unlike iron chalcogenides, LiFeAs has a single phase and has no complication of magnetic or orbital long-range orders at low temperature [19]. Last but not least, first-principles calculations find that although the strength of the Hund's coupling J_H is similarly strong in iron pnictides and iron chalcogenides [11], the band renormalization factor on the holelike d_{xy}

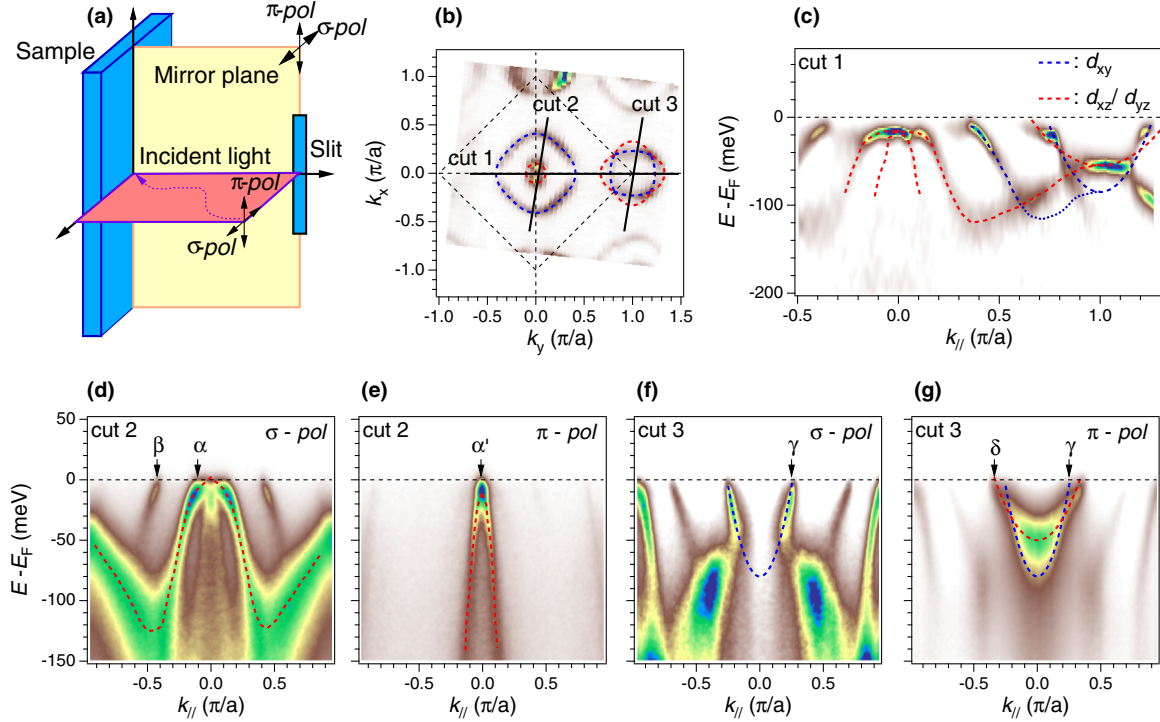*p.richard@aphy.iphy.ac.cn
†dingh@iphy.ac.cn

FIG. 1. (a) Experimental setup of the polarization measurements. The π polarization (π-pol) is pure, whereas the σ polarization (σ-pol) is mixed with c-axis polarization. (b) FS mapping at 74 eV with σ-pol. Dashed lines are the extracted FSs. The blue and red colors represent d_{xy} and $d_{xz/yz}$ orbitals, respectively. (c) Curvature of ARPES intensity of cut 1. The red and blue dashed dispersions are extracted from the high-resolution polarization data shown in (d)–(g).

band is two to three times smaller in the iron pnictides than in the iron chalcogenides. The similarities and differences between the pnictides and the chacolgenides are important for identifying the key correlations in all FeSCs, which are vital to understand the emergence of superconductivity and its pairing symmetry.

The electronic structure of LiFeAs consists of five bands near the Fermi energy (E_F) with three hole bands at the Brillouin zone (BZ) center and two electron bands at the corner of the 2 Fe/unit cell BZ. In order to determine their main orbital characters, we employ linearly polarized light to the mirror plane of the samples, as shown in Fig. 1(a). Under this geometry, the π polarization (π-pol) is pure and selects orbitals that have an even symmetry with respect to the mirror plane, while the σ polarization (σ-pol) is mixed with the c-axis polarization, hence selecting orbitals that have an odd symmetry as well as d_{z^2} and p_z orbitals [20]. Figure 1(b) shows the Fermi surface (FS) mapping at 74 eV with the σ-pol, the red and blue dashed lines corresponding to the extracted FSs. The curvature of the ARPES intensity of cut 1 is displayed in Fig. 1(c). The red and blue dashed dispersions are extracted from the high-resolution polarization measurements shown in Figs. 1(d)–1(g). In agreement with previous ARPES studies [18,21], we find that the orbital components of the α, α', β, and δ bands are relatively pure and mainly composed of $d_{xz/yz}$, $d_{xz/yz}$, d_{xy}, and $d_{xz/yz}$ orbitals, respectively. The γ band, however, is a mix of the d_{xy} and $d_{xz/yz}$ orbitals, as it can be clearly seen from both the σ-pol and π-pol geometries. We note that while the t_{2g} orbitals (d_{xy}, d_{xz}, d_{yz}) have the largest contributions to the density of states near E_F, all bands are

slightly mixed with the e_g ($d_{x^2-y^2}, d_{z^2}$) and p orbitals except at the Γ and M high-symmetry points.

To prove the existence of well-defined QPs, we look at the well-isolated β band, which has the largest band renormalization factor (about 4) and effective mass (about $8m_e$, where m_e is the free electron mass) among all five bands [22,23]. Figure 2(a) shows the normal state ARPES intensity plot of the β band at 20 K. Selected energy/momentum distribution curves (EDCs/MDCs) of the β band shown in Figs. 2(b) and 2(c) are labeled by the colored circles in Fig. 2(a). Following common practice [1,3], we extracted the energy-dependent scattering rates $\Gamma_k(\omega)$ and the renormalization factor $Z_k(\omega)$ of the β band from MDCs, and plotted them in Figs. 2(d) and 2(e), respectively. The extracted scattering rate near E_F is dominated by the thermal broadening of the QP lifetime convoluted with our experimental energy and momentum resolutions, and lies deep in the Landau's QP regime, where Im $\Sigma_k(\omega) < \omega$, hence proving the existence of well-defined QPs in LiFeAs. The red shaded area represents the nonquasiparticle regime. The area does not go to zero because of the temperature correction $\pi k_B T$ to the self-energy. The 16 meV anomalies observed in both $\Gamma_k(\omega)$ and $Z_k(\omega)$ are likely induced by electron-boson couplings with negligible contributions of the antiferromagnetic spin resonance [22].

Now we turn to the temperature dependence of the QPs. Figures 3(a)–3(e) show ARPES intensity plots of the β band at 30, 50, 100, 150, and 200 K, respectively. Figures 3(f)–3(j) show the temperature evolution of the γ and δ bands. To reveal the electronic states above E_F, all spectra are divided by the Fermi-Dirac function convoluted with the system
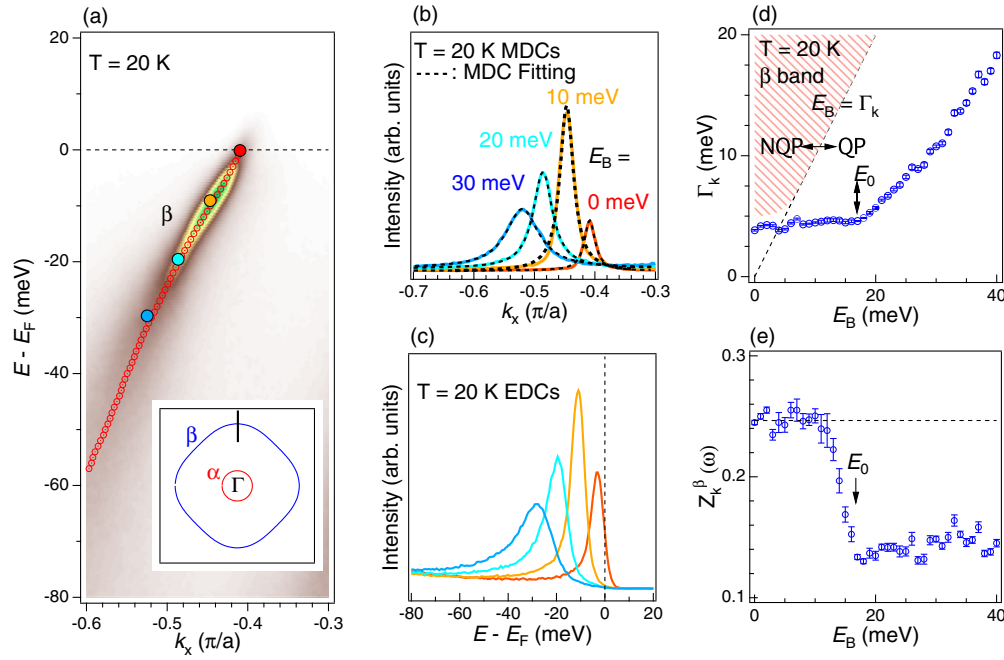
FIG. 2. (a) ARPES intensity plot of the β band at 20 K. EDCs/MDCs that are crossing the colored circles in (a) are shown in (b) and (c). Black dashed curves in (b) are single Lorentz function fittings. (d) Extracted energy-dependent scattering rates Im $\Sigma(\omega)$ are represented by blue circles. The red shaded area represents the nonquasiparticle regime. The area does not go to zero because of the temperature correction $\pi k_B T$ to the self-energy. (e) Extracted energy-dependent renormalization factor of the β band. E_0 at 16 meV shown in (d) and (e) corresponds to the energy of the spectral function anomaly [22]. Error bars are determined by the standard deviation of the fitting parameters.

resolution. As shown in Figs. 3(a)– 3(e), the β band, which is mainly composed of a d_{xy} orbital character, dramatically loses intensity and is nearly invisible at 200 K, while the δ band, which is mainly composed of a $d_{xz/yz}$ orbital, becomes broader and its intensity remains relatively strong even at 200 K. This orbital-dependent intensity loss is consistent with a previous report on the same material, where the drop in peak intensity on the β band is much faster than it is on the α and α' bands, which are mainly composed of a $d_{xz/yz}$ orbital [13,22]. We shall note that previous studies found an orbital fluctuation or spin-orbit coupling-induced band splitting between the α and α' band, however, this splitting is not observed at the M point in LiFeAs. Since the splitting, if present at the M point, is much smaller (<3 meV) than the bandwidth (hundreds meV), it will not change the spectral function evolution within our experimental uncertainties. In Fig. 3, we show the DFT+DMFT calculated hole bands [Figs. 3(k)–3(m)] and electron bands [Figs. 3(n)–3(p)] at several temperatures. The overall momentum- and energy-resolved spectra agree quite well with experimental measurements without any adjustment such as band renormalization and shift, which are usually needed for the DFT band structure, validating the DFT+DMFT approach. It is also evident that the DFT+DMFT intensity of the β band with a d_{xy} orbital is substantially weaker than the $d_{xz/yz}$ bands at 232 K [22], which is consistent with the experimental observations [22].

In order to quantitatively compare the difference between the β band and the δ band, we analyze the measured EDCs at k_F^{β} and k_F^{δ}, which are marked by blue and red lines in Figs. 3(a) and 3(f), respectively. In Figs. 4(a) and 4(b), we show the

EDCs of the β band and the δ band from 20 to 200 K. All curves are fitted by the QP spectral function plus a polynomial background, and the extracted QP peaks of the β and the δ bands are plotted in Figs. 4(d) and 4(e), respectively [22]. The temperature-dependent QP scattering rates are extracted and plotted in Fig. 4(c). The gray shaded background represents the coherence-incoherence crossover regime where the derivative of the resistivity curve reaches a maximum and starts to drop [24]. Interestingly, in agreement with a recent study [25], we find that the QP scattering rates on both the β band and the δ band also severely deviate from their low-temperature T-quadratic behavior near this temperature, indicating that the saturation of resistivity is intimately connected to the high-temperature QP scattering rate.

Although the scattering rates of the β band and the δ band show similar temperature evolutions, we find that the total spectral weights (TSWs) of the β and δ bands have different behaviors at high temperature. To extract the spectral weight (SW), we integrate the extracted and DFT+DMFT calculated QP spectral functions shown in Figs. 4(d) and 4(e) [22] and plot the integrated SW of the β and δ bands in Fig. 4(f). Both the experimental data and the theoretical calculations show a nearly conserved SW on the δ band up to 200 K, and a dramatically reduced SW on the β band at high temperature [22]. Indeed, the intensity change of the α and α' is similar to the δ band and much slower than the β band with increasing temperature [13,22], further proving the change of SW is orbital dependent.

This orbital-dependent SW reduction with elevated temperature is fully consistent with the Hund's metal picture where an
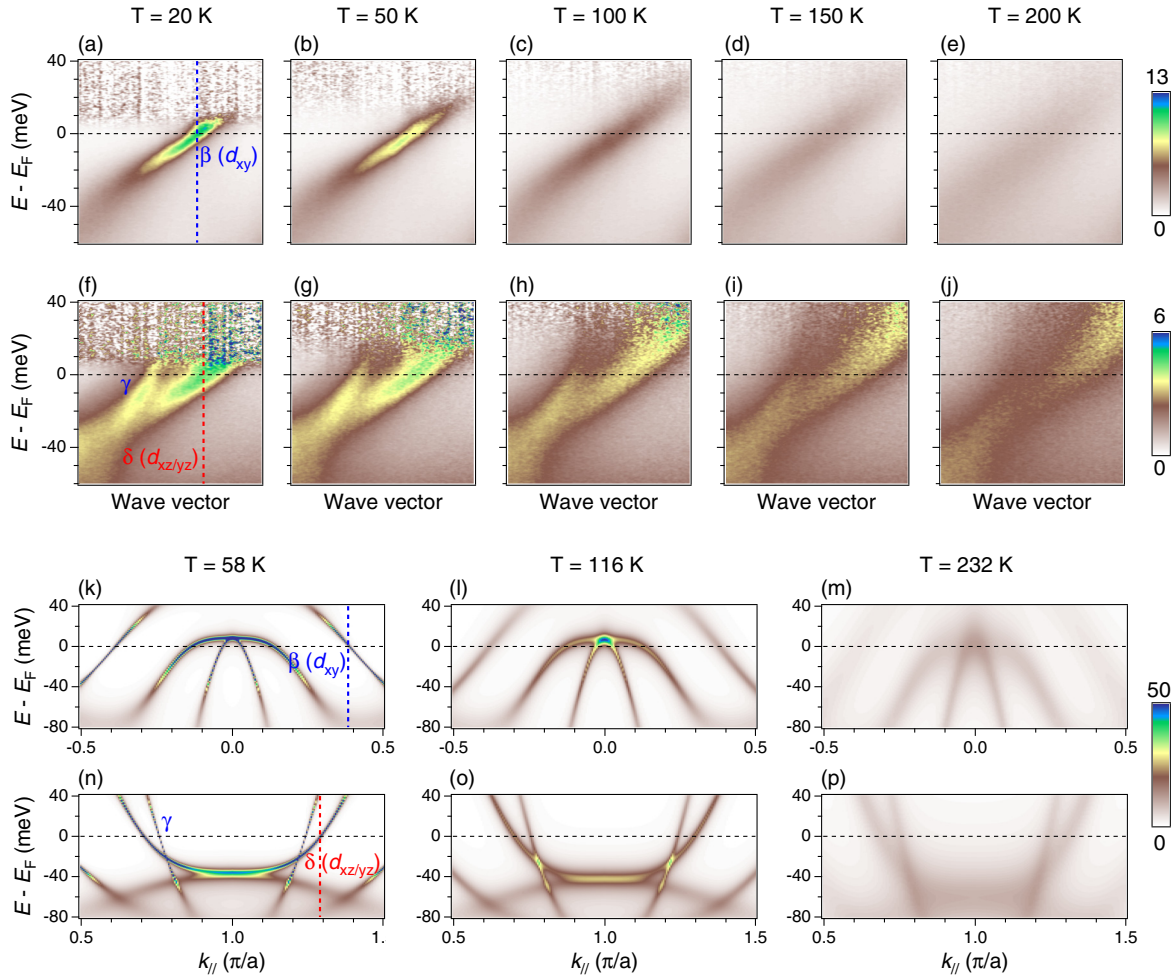
FIG. 3. (a)–(e) ARPES intensity plots of the β band at 30, 50, 100, 150, and 200 K, respectively. (f)–(j) ARPES intensity plots of the δ and γ bands at 30, 50, 100, 150, and 200 K, respectively. All spectra are divided by the Fermi-Dirac function convoluted with the system resolution. (k)–(p) DFT+DMFT calculated momentum- and energy-resolved spectral function at 58, 116, and 232 K. (k)–(m) and (n)–(p) correspond to hole bands and electron bands, respectively.

orbital-differentiated coherence-incoherence crossover occurs at different temperatures due to the strong Hund's rule coupling [26,27]. This is further supported by a recent DMFT plus numerical renormalization group study confirming that the iron pnictides are Fermi liquids at low temperature, and the orbital-differentiated coherence-incoherence crossover is driven by a Kondo-type screening with the Kondo temperature determined by the strength of Hund's coupling [28]. In the Hund's metal point of view, both iron pnictides and iron chalcogenides have a Hund-differentiated coherence-incoherence crossover. Indeed, previous studies [7,8] show that both FeTe and $K_x Fe_{2-y} Se_2$ exhibit a similar orbital-differentiated coherence-incoherence crossover, with the d_{xy} orbital having the lowest coherent temperature. Therefore, our work proves that the orbital-differentiated coherence-incoherence crossover is a generic feature of FeSCs. Moreover, this phenomenon is not limited to FeSCs but is a common feature of all Hund's metals [27], such as the ruthenates.

Previously, it was also proposed that FeSCs are in close proximity to a Mott state [9,10]. The orbital-dependent SW reduction upon increasing temperature was interpreted as the materials undergoing an orbital-selective Mott transition with

the d_{xy} orbital being the insulating orbital. Although in this picture the SW will decrease if the system goes towards the orbital-selective Mott state by tuning some parameters, the hybridization of the insulating orbital (d_{xy}) with all other orbitals ($d_{xz/yz}$) must vanish to achieve an orbital-selective Mott state [22]. However, both local density approximation (LDA) calculations and experimental data clearly show hybridization between the d_{xy} orbital and the $d_{xz/yz}$ orbital in LiFeAs is of about 150–300 meV [21,25]. This suggests that LiFeAs is far away from the proposed orbital-selective Mott state and reinstates the Hund's coupling-induced orbital-differentiated coherence-incoherence crossover viewpoint, in which the reduced spectral weight upon increasing temperature dissolves into an incoherent background with a finite density of states at the Fermi level at high temperature due to the strong Hund's coupling J_H and the Kondo-screening mechanism, which leads to the decoupling of the orbital and spin degrees of freedom at high temperatures. Our results, together with previous studies on iron chacolgenides, show that the orbital-differentiated coherence-incoherence crossover is a phenomenon ubiquitous to all FeSCs, and more generally to all Hund's metals whose physics is mainly controlled by the strength of the Hund's coupling.
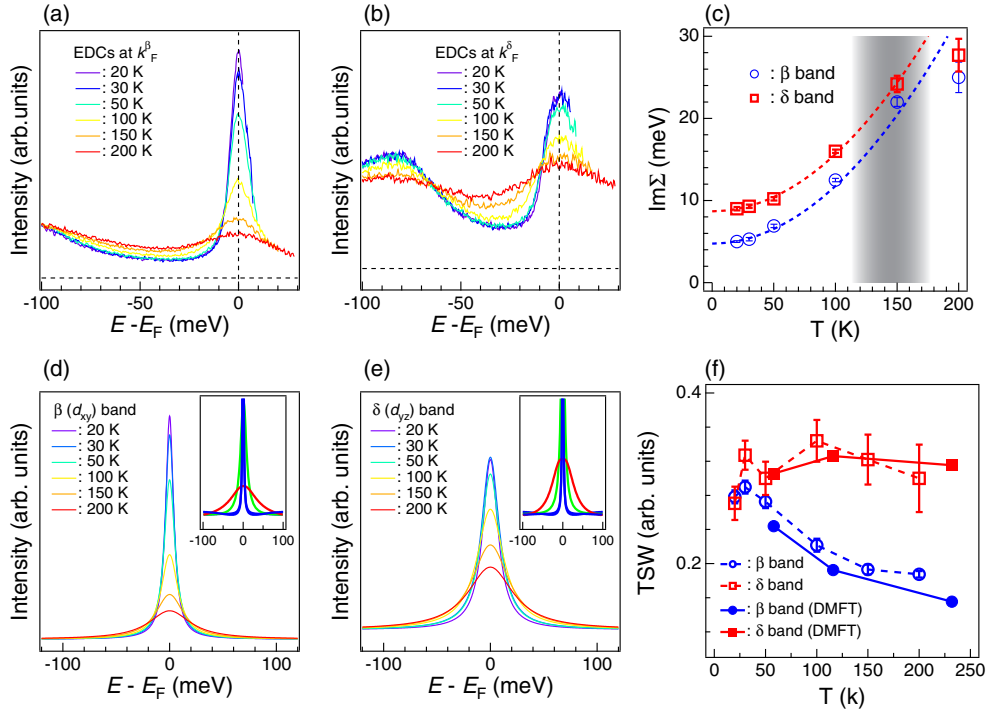
FIG. 4. (a) and (b) EDCs of the β and δ bands from 20 to 200 K. All curves are fitted by the QP spectral function plus a polynomial background [22]. The horizontal dashed lines represent zero intensity. (c) Extracted temperature-dependent QP scattering rates. The gray shaded background represents the maximum region of the derivative of the resistivity curve. (d) and (e) Extracted QP peaks at k_F^β and k_F^δ, respectively. The insets of (d) and (e) are DFT+DMFT calculated spectral functions at k_F^β and k_F^δ, respectively. To get the total QP spectral weight, we integrate the extracted and calculated spectral functions shown in (d) and (e) and plot the results in (f). Error bars shown in (c) and (f) are determined by the standard deviation of the fitting parameters.

[1] P. D. Johnson, T. Valla, A. V. Fedorov, Z. Yusof, B. O. Wells, Q. Li, A. R. Moodenbaugh, G. D. Gu, N. Koshizuka, C. Kendziora, S. Jian, and D. G. Hinks, Phys. Rev. Lett. **87**, 177007 (2001).

[2] A. Damascelli, Z. Hussain, and Z.-X. Shen, Rev. Mod. Phys. **75**, 473 (2003).

[3] T. Valla, A. V. Fedorov, P. D. Johnson, and S. L. Hulbert, Phys. Rev. Lett. **83**, 2085 (1999).

[4] P. Richard, T. Sato, K. Nakayama, S. Souma, T. Takahashi, Y.-M. Xu, G. F. Chen, J. L. Luo, N. L. Wang, and H. Ding, Phys. Rev. Lett. **102**, 047003 (2009).

[5] M. R. Norman, H. Ding, J. C. Campuzano, T. Takeuchi, M. Randeria, T. Yokoya, T. Takahashi, T. Mochiku, and K. Kadowaki, Phys. Rev. Lett. **79**, 3506 (1997).

[6] M. R. Norman, M. Randeria, H. Ding, and J. C. Campuzano, Phys. Rev. B **57**, R11093 (1998).

[7] M. Yi, D. H. Lu, R. Yu, S. C. Riggs, J.-H. Chu, B. Lv, Z. K. Liu, M. Lu, Y.-T. Cui, M. Hashimoto, S.-K. Mo, Z. Hussain, C. W.

Chu, I. R. Fisher, Q. Si, and Z.-X. Shen, Phys. Rev. Lett. **110**, 067003 (2013).

[8] M. Yi, Z.-K. Liu, Y. Zhang, R. Yu, J.-X. Zhu, J. J. Lee, R. G. Moore, F. T. Schmitt, W. Li, S. C. Riggs, J.-H. Chu, B. Lv, J. Hu, M. Hashimoto, S.-K. Mo, Z. Hussain, Z. Q. Mao, C. W. Chu, I. R. Fisher, Q. Si, Z.-X. Shen, and D. H. Lu, Nat. Commun. **6**, 7777 (2015).

[9] R. Yu and Q. Si, Phys. Rev. B **84**, 235115 (2011).

[10] L. de' Medici, G. Giovannetti, and M. Capone, Phys. Rev. Lett. **112**, 177001 (2014).

[11] Z. P. Yin, K. Haule, and G. Kotliar, Nat. Mater. **10**, 932 (2011).

[12] Z. P. Yin, K. Haule, and G. Kotliar, Nat. Phys. **7**, 294 (2011).

[13] H. Miao, L.-M. Wang, P. Richard, S.-F. Wu, J. Ma, T. Qian, L.-Y. Xing, X.-C. Wang, C.-Q. Jin, C.-P. Chou, Z. Wang, W. Ku, and H. Ding, Phys. Rev. B **89**, 220503 (2014).

[14] K. Haule, C.-H. Yee, and K. Kim, Phys. Rev. B **81**, 195107 (2010).

[15] G. Derondeau, F. Bisti, J. Braun, V. A. Rogalev, M. Shi, T. Schmitt, J. Z. Ma, H. Ding, H. Ebert, V. N. Strocov, and J. Minar, arXiv:1606.08977.

[16] Z. P. Yin, K. Haule, and G. Kotliar, Nat. Phys. **10**, 845 (2014).

[17] H. Miao, T. Qian, X. Shi, P. Richard, T. K. Kim, M. Hoesch, L. Y. Xing, X.-C. Wang, C.-Q. Jin, J.-P. Hu, and H. Ding, Nat. Commun. **6**, 6056 (2015).

[18] Z. R. Ye, Y. Zhang, F. Chen, M. Xu, J. Jiang, X. H. Niu, C. H. P. Wen, L. Y. Xing, X. C. Wang, C. Q. Jin, B. P. Xie, and D. L. Feng, Phys. Rev. X **4**, 031041 (2014).

[19] Y. M. Dai, H. Miao, L. Y. Xing, X. C. Wang, P. S. Wang, H. Xiao, T. Qian, P. Richard, X. G. Qiu, W. Yu, C. Q. Jin, Z. Wang, P. D. Johnson, C. C. Homes, and H. Ding, Phys. Rev. X **5**, 031035 (2015).

[20] X.-P. Wang, P. Richard, Y.-B. Huang, H. Miao, L. Cevey, N. Xu, Y.-J. Sun, T. Qian, Y.-M. Xu, M. Shi, J.-P. Hu, X. Dai, and H. Ding, Phys. Rev. B **85**, 214518 (2012).

[21] S. V. Borisenko, V. B. Zabolotnyy, D. V. Evtushinsky, T. K. Kim, I. V. Morozov, A. N. Yaresko, A. A. Kordyuk, G. Behr, A. Vasiliev, R. Follath, and B. Büchner, Phys. Rev. Lett. **105**, 067002 (2010).

[22] See Supplemental Material at http://link.aps.org/supplemental/10.1103/PhysRevB.94.201109 for additional details of data analysis and theoretical support.

[23] J. Ferber, K. Foyevtsova, R. Valentí, and H. O. Jeschke, Phys. Rev. B **85**, 094505 (2012).

[24] A. F. Kemper, M. M. Korshunov, T. P. Devereaux, J. N. Fry, H.-P. Cheng, and P. J. Hirschfeld, Phys. Rev. B **83**, 184516 (2011).

[25] V. Brouet, D. LeBoeuf, P.-H. Lin, J. Mansart, A. Taleb-Ibrahimi, P. Le Fèvre, F. Bertran, A. Forget, and D. Colson, Phys. Rev. B **93**, 085137 (2016).

[26] Z. P. Yin, K. Haule, and G. Kotliar, Phys. Rev. B **86**, 195141 (2012).

[27] J. Mravlje, M. Aichhorn, T. Miyake, K. Haule, G. Kotliar, and A. Georges, Phys. Rev. Lett. **106**, 096401 (2011).

[28] K. M. Stadler, Z. P. Yin, J. von Delft, G. Kotliar, and A. Weichselbaum, Phys. Rev. Lett. **115**, 136401 (2015).